

Multimodality for improved CNN photometric redshifts

R. Ait Ouahmed^{1*}, S. Arnouts¹, J. Pasquet^{2,3}, M. Treyer¹, and E. Bertin⁴

¹ Aix Marseille Univ, CNRS, CNES, LAM, Marseille, France

² AMIS - Université Paul-Valéry - Montpellier 3

³ UMR TETIS - INRAE, AgroParisTech, Cirad, CNRS, Montpellier, France

⁴ Sorbonne Université, CNRS, UMR 7095, Institut d'Astrophysique de Paris, 98 bis bd Arago, 75014 Paris, France

Received date; accepted date

ABSTRACT

Photometric redshift estimation plays a crucial role in modern cosmological surveys for studying the universe's large-scale structures and the evolution of galaxies. Deep learning has emerged as a powerful method to produce accurate photometric redshift estimates from multi-band images of galaxies. Here, we introduce a multimodal approach consisting of the parallel processing of several subsets of image bands prior, the outputs of which are then merged for further processing through a convolutional neural network (CNN). We evaluate the performance of our method using three surveys: the Sloan Digital Sky Survey (SDSS), The Canada-France-Hawaii Telescope Legacy Survey (CFHTLS) and Hyper Suprime-Cam (HSC). By improving the model's ability to capture information embedded in the correlation between different bands, our technique surpasses the state-of-the-art photometric redshift precision. We find that the positive gain does not depend on the specific architecture of the CNN and that it increases with the number of photometric filters available.

Key words. Galaxies: distances and redshifts – Galaxies: photometry – surveys – catalogs

1. Introduction

Photometric redshifts have become crucial for cosmological surveys based on multi-band imaging surveys such as the current Dark Energy Survey (DES; DES Collaboration et al. 2016), the Kilo-Degree Survey (KIDS, de Jong et al. 2013) and the upcoming Vera Rubin survey (LSST, Ivezić et al. 2019) and Euclid (Laureijs et al. 2011). The magnitude depth and the extent of the area covered by these surveys make it impossible to rely solely on spectroscopy for redshift estimates, so that, photometric redshifts became a major component of these cosmological endeavors.

The methods to estimate redshifts from multi-band photometry fall in three broad categories:

- Spectral Energy Distribution (SED) template fitting: this technique has been used for several decades. It relies on a set of observed or modeled SEDs, assumed to be representative of the diversity of galaxies. These theoretical magnitudes are then compared to the observed ones with a minimization fitting procedure to derive the most probable template and redshift estimates (e.g. Arnouts et al. 1999; Ilbert et al. 2006; Benítez 2000; Brammer et al. 2008).
- Machine Learning algorithms: this approach benefits from the increase in available spectroscopic redshifts required to train the algorithms. Models learn correlations between redshift and the input features provided. Once trained, they can be used to estimate redshifts based on the same input information. Different algorithms have been used such as artificial neural network (Collister & Lahav 2004), k -Nearest Neighbors (kNN, Csabai et al. 2007) or random forest techniques (Carliles et al. 2010). These methods are fast and were shown to be effective in the domain of validity of the training set.

As with SED fitting algorithms, the input information consists of features extracted from the multi-band images, such as fluxes, colors, and morphological parameters.

- Deep learning algorithms: the images are used directly as input, in contrast to the two previous methods. These algorithms are multiple-layer neural networks that extract relevant features from the multi-band images of galaxies by adjusting parameters during a learning process where a cost function is minimized. Convolutional Neural Networks (CNNs) are a popular type of deep learning algorithm for image-related tasks. CNNs are designed to detect small, local correlations and patterns in images with the first layers, and increasingly larger and more complex patterns with deeper layers.

Over the last few years, deep learning has proven to be a highly effective method. Through the use of various deep learning frameworks, state of the art results have been achieved in photometric redshift estimation in the Main Galaxy Sample of the Sloan Digital Sky Survey (SDSS MGS), a nearly complete spectroscopic dataset to $r = 17.8$.

Pasquet et al. (2019) (hereafter P19) developed a deep CNN based on the Inception network. The method uses 64×64 pixel images centered on the SDSS spectroscopic targets in the *ugriz* bands, along with the line-of-sight galactic reddening value. The results show an improvement by a factor of 1.5 over the released SDSS photometric redshifts, which are based on a k -NN algorithm (Beck et al. 2016).

Hayat et al. (2021) presented a self-supervised contrastive learning framework. It aims to build a low dimensional space that captures the underlying structure and meaningful features of a large dataset of unlabeled (no spectroscopic redshift) galaxies. The network is trained to minimize the distance between representations of a source image and its augmented versions while

* e-mail: reda.ait-ouahmed@lam.fr

maximizing the distance between these representations and representations of other galaxies. Once this latent space is obtained, the network is fine-tuned on the redshift estimation task with labeled data. This work outperforms P19 but more interestingly, it reveals that including unlabeled data reduces the amount of labeled data necessary to achieve the P19 results.

Dey et al. (2021) used Deep Capsule Networks to jointly estimate redshift and morphological type. Their network consists of a primary convolutional layer followed by Conv-Caps layers. While conventional CNNs primarily detect features, capsule networks also compute feature properties (orientation, size, colors, etc.). Note that even though these networks are robust and invariant to image orientation, the authors used rotation and flip data augmentation during training. The dimension of their latent space is only 16, which allows for a better interpretability. Compared to classical CNNs, the capsule networks are more difficult to train, and not easy to scale to deeper architectures for more complex tasks. Their results on the SDSS sample show a marginal improvement over P19.

Finally, Treyer et al. (2023, submitted) present an updated version of the network introduced by P19. The number of parameters is reduced with a latent space of 96 dimensions instead of 22272 in the original work, which improves the generalization capacity of the network. While their goal is to extend redshift estimation to fainter magnitude, they also show that the new network outperforms previous works on the SDSS MGS (see Table. 2).

In this work, we propose a multimodal architecture. Multimodality commonly refers to the combination of different types of information for training (Ngiam et al. 2011; Ma et al. 2015; Hou et al. 2018). This approach is especially relevant when dealing with data from different sensors (such as cameras, LiDAR, and radar). It exploits the complementary nature of the information contained in different types of data (e.g., Qian et al. 2021; Chen et al. 2017) by processing them in parallel modalities, allowing them to interact at various stages and finally merging them all together (Hong et al. 2020).

The photometric images provide a low-resolution view of the source spectra, and the correlation between them is strongly informative of the redshift. The conventional approach is to stack these images all together as a network input (P19, Hayat et al. (2021); Dey et al. (2021); Treyer et al. (2023)). In this work, we show that this is suboptimal and we introduce the use of multimodality for redshift estimation. It consists in organizing the input into subsets of bands that are processed in parallel prior to being merged, which improves the extraction of inter-band correlations, and ultimately the redshift precision. Furthermore, we discuss the key ingredients of the multimodal architecture and validate it on several datasets.

The paper is organized as follows: the different photometric and spectroscopic datasets are presented in Section 2; the architecture, training and input/output of the network are described in Section 3, with additional information in Appendix A; the adaptation of the network to incorporate multimodality is described in Section 4; Section 5 defines the metrics used to evaluate the redshift estimates and presents different experiments to understand the key components of the multimodal approach; Section 6 presents the performance and gains of the optimal multimodal network with respect to the baseline model (single modality) on different datasets; discussions are made in Section 7 and we conclude this work in Section 8.

2. Data

We use three different photometric and spectroscopic datasets covering a wide range of image depth and redshift. In the following, DR stands for Data Release.

2.1. The SDSS survey

The SDSS is a 5-band (*ugriz*) imaging ($r \leq 22.5$) and spectroscopic survey using a dedicated 2.5-meter telescope at Apache Point Observatory in New Mexico. We use the same spectroscopic sample as P19 based on the SDSS DR12 (Alam et al. 2015) in the northern galactic cap and Stripe82 regions. It consists of 516,525 sources with dereddened petrosian magnitudes $r \leq 17.8$ and spectroscopic redshifts $z \leq 0.4$. For each source, in each of the 5 bands, all the available images from the SDSS Science Archive Server are resampled, stacked and clipped. The resulting input data is a $5 \times 64 \times 64$ pixel datacube with a pixel scale of 0.396 arcsec, in a gnomonic projection centered on the galaxy coordinates, and aligned with the local celestial coordinate system (see P19 for details), in addition to the galactic extinction value (Schlegel et al. 1998).

2.2. The CFHTLS imaging survey

The Canada-France-Hawaii Telescope (CFHT) Legacy Survey¹ (CFHTLS) is an imaging survey performed with MegaCam (Boulade et al. 2000) in five optical bands (u^*griz). In the following we only considered the CFHTLS-Wide component, which covers four independent sky patches totaling 154 deg^2 with sub-arcsecond seeing (median $\sim 0.7''$) and a typical depth of $i \sim 24.8$ (5σ detection in 2" apertures).

We use the images and photometric catalogues from the T0007 release² produced by TERAPIX³ (Hudelot et al. 2012). This final release includes an improved absolute and internal photometric calibration, at a 1-2% level, based on the photometric calibration scheme adopted by the Supernova Legacy Survey (SNLS Regnault et al. 2009).

The final images are stacked with the Swarp tool⁴ (Bertin 2006). The detection and photometric catalogues were performed with SExtractor (Bertin & Arnouts 1996) in dual mode with the source detection based on the $gri - \chi^2$ image (Szalay et al. 1999). Although the pixel scale is smaller (i.e., 0.18 arcsec/pix) than in the SDSS, we adopt the same 64×64 pixel cutouts for the CFHTLS datacubes.

2.3. The HSC-Deep imaging survey

This dataset consists of the four HSC-Deep fields (COSMOS, XMM-LSS, ELAIS-N1 and DEEP2-3) partially covered by the *u*-band CLAUDS survey (Sawicki et al. 2019) and the near-infrared (NIR) surveys UltraVISTA (McCracken et al. 2012, COSMOS field) and VIDEO (Jarvis et al. 2013, XMM-LSS field). A full description of the HSC-Deep dataset and its ancillary data are detailed in Desprez et al. (2023) and summarized hereafter.

The HSC-SSP is an imaging survey conducted with the Hyper Suprime-Cam camera (Miyazaki et al. 2018) on the Sub-

¹ <http://www.cfht.hawaii.edu/Science/CFHTLS/>

² <http://terapix.iap.fr/cplt/T0007/doc/T0007-doc.html>

³ <http://terapix.iap.fr/>

⁴ <http://astromatic.net/software/swarp>

Spectroscopy			
Survey	Res.	z-range	Selection
SDSS DR12 ⁽¹⁾	2000	$z \leq 0.4$	$r \leq 17.8$
SDSS-BOSS ⁽²⁾	2000	$0.3 \leq z \leq 0.7$	LRGs
GAMA ⁽³⁾	1300	$z \leq 0.7$	$r \leq 19.8$
WIGGLEZ ⁽⁴⁾	1300	$z \leq 1.2$	$NUV \leq 22.8$
zCOSMOS ⁽⁵⁾	650	$z \leq 1.2-5$	$r \leq 22.5 - 25$
VANDELS ⁽⁶⁾	650	$1 \leq z \leq 6$	$H \leq 25$
UDSz ⁽⁷⁾	650	$z \leq 4$	$K \leq 23$
DEEP2 ⁽⁸⁾	6000	$0.7 \leq z \leq 1.5$	$r \leq 24$
VVDS ⁽⁹⁾	230	$z \leq 1.2-6$	$i \leq 22.5 - 24$
VIPERS ⁽¹⁰⁾	230	$0.4 \leq z \leq 1.5$	$i \leq 22.5$
VUDS ⁽¹¹⁾	230	$2 \leq z \leq 6$	$K \leq 23$
CLAMATO ⁽¹²⁾	1100	$2 \leq z \leq 3.5$	LBGs
C3R2 ⁽¹³⁾	1100	$z \leq 4$	SOM
COSMOS ⁽¹⁴⁾	multiple	$z \leq 4$	multiple
3DHST ⁽¹⁵⁾	130	$z \leq 4$	$H \leq 24$
PRIMUS ⁽¹⁶⁾	40	$z \leq 0.9$	$i \leq 22.5$
COSMOS20 ⁽¹⁷⁾	photo-z	$z \leq 6$	$i \leq 26.5$

Table 1: Summary of the spectroscopic surveys with their typical spectral resolution, redshift range and main target selection criteria. Surveys 1 to 14 are used for the spectroscopic training/validation datasets. Survey 15 to 17 are used for test only.

aru telescope in 5 broadband filters (*grizy*)⁵. We use the public DR2 (Aihara et al. 2019) for the Deep ($\sim 20 \text{ deg}^2$) and Ultra-Deep ($\sim 3 \text{ deg}^2$) layers of the survey. These have median depths $g = 26.5 - 27$ and $y = 24.5 - 25.5$ respectively.

CLAUDS is a deep survey with the CFHT MegaCam imager in the *u*-band and slightly redder *u**-band (Sawicki et al. 2019). The *u** filter covers the whole XMM-LSS region. ELAIS-N1 and DEEP2-3 are exclusively covered with the *u* filter, while COSMOS was observed with both filters. CLAUDS covers 18 deg^2 of the four HSC-Deep fields down to a median depth $u = 27$, and 1.6 deg^2 of the two ultra-deep regions down to $u = 27.4$.

UltraVISTA⁶ and VIDEO⁷ are deep NIR surveys acquired by the VISTA Telescope (Emerson et al. 2004) with the VIRCAM instrument (Dalton et al. 2006). For UltraVISTA we use the DR3 *YJHK_s* images covering 1.4 deg^2 down to $Y \sim 25$ and $J, H, K_{s} \sim 24.7}$ (McCracken et al. 2012).

For VIDEO we use the DR4 images in the same passbands covering 4.1 deg^2 , down to depths ranging from $Y = 25.0$ to $K_{s} = 23.8}$ (Jarvis et al. 2013).

All the images are projected onto the same HSC reference pixel grid, using SWARP (Bertin et al. 2002), with a pixel scale of $0.168''/\text{pixel}$. For the *u*-band images, the stacks are generated with the native HSC pixel grid, while for the NIR images the fully calibrated mosaics are later projected onto the HSC pixel grid.

The dimension of the HSC-Deep datacubes is $9 \times 64 \times 64$ pixels. They include one *u*-band image (*u**, otherwise *u*), five HSC images (*grizy*) and three NIR images (*JHK_s*). When missing, the NIR channels are padded with zeros.

⁵ The HSC-Deep survey include also narrowband filters not considered in this work

⁶ <https://ultravista.org>

⁷ http://www.eso.org/sci/observing/phase3/data_releases.html

2.4. The spectroscopic redshift dataset

The CFHTLS and HSC-Deep regions have been widely covered by large spectroscopic redshift surveys, including: SDSS-BOSS (DR16, available everywhere, Ahumada et al. 2020), GAMA (DR3, $r \leq 19.8$, Baldry et al. 2018), WiggleZ (final release, $NUV \leq 22.8$, Drinkwater et al. 2018), VVDS Wide and Deep ($i \leq 22.5$ and $i \leq 24$, Le Fèvre et al. 2013), VUDS ($i \leq 25$, Le Fèvre et al. 2015), DEEP2 (DR4, $r \leq 24$, Newman et al. 2013), VIPERS (DR2, $i \leq 22.5$, Scodreggio et al. 2018), VANDELS (DR4, high redshift in XMM-LSS, $H \leq 25$, Garilli et al. 2021), CLAMATO (DR1, high redshift LBGs in COSMOS, Lee et al. 2018), UDSz (in XMM-LSS, McLure et al. 2013; Bradshaw et al. 2013) and zCOSMOS-bright ($i \leq 22.5$ in COSMOS, Lilly et al. 2007). We also include the COSMOS team's spectroscopic redshift catalog (M. Salvato, private communication), which consists of several optical and NIR spectroscopic follow-ups of X-ray to far-IR/radio sources, high-redshift star-forming and passive galaxies, as well as poorly represented galaxies in multidimensional color space (C3R2, Masters et al. 2019). The Table 1 summarizes the main characteristics of the different spectroscopic surveys considered.

For all the above redshift surveys, we only consider the most secure redshifts, identified with high signal-to-noise and several spectral features (equivalent to flags 3 and 4 in VVDS or VIPERS). For duplicated redshifts, we keep the most secure or randomly pick up one when they have similar flag quality.

The characteristics of the spectroscopic samples associated to each photometric survey are as follows:

- The SDSS sample includes 516,525 sources with $r \leq 17.8$ and spectroscopic redshifts $z \leq 0.4$.
- The CFHTLS-Wide sample includes $\sim 108,500$ secure redshifts distributed as 34% with $i \leq 19.5$, 57% with $19.5 \leq i \leq 22.5$ and 9% with $22.5 \leq i \leq 25$.
- The HSC-Deep survey includes $\sim 51,000$ redshifts with at least six optical bands (*ugrizy*) and 45% are brighter than $i \sim 22$ and 10% fainter than $i \sim 24$. Amongst this sample, $\sim 37,400$ sources also have NIR bands (*JHK_s*).

In addition, for the HSC-Deep survey, we also include as test samples the low-resolution spectroscopic redshifts from the 3DHST survey (based on NIR slitless grism spectroscopy, Skelton et al. 2014), the PRIMUS survey (based on optical prism multi-objects spectroscopy, Coil et al. 2011), and the 30 band photometric redshifts from COSMOS2020 (Weaver et al. 2022), with the spectral resolution reported in Table 1.

- For 3DHST, we use the DRv4.1.5 restricted to secure grism redshift measurement (Momcheva et al. 2016; Skelton et al. 2014). It contains $\sim 4,150$ sources with $H_{AB} \leq 24$ located in XMM-LSS and COSMOS.
- For PRIMUS, we restrict the sample to bright sources ($i_{AB} \leq 22.5$) at moderate redshift ($z \leq 0.9$) with the most secure redshifts (Cool et al. 2013). It contains $\sim 19,500$ sources, located in XMM-LSS, COSMOS and DEEP2-3 fields.
- For COSMOS2020, we use the 30 band photometric redshifts provided by Weaver et al. (2022), who estimated four different photometric redshifts based on two different multi-band photometric catalogues (using two distinct flux extraction software packages) and two different photometric redshift codes. We compute the mean and standard deviation of these 4 redshifts, \bar{z} and $\sigma(z)$, and retain those with $\sigma(z) \leq 0.1(1 + \bar{z})$.

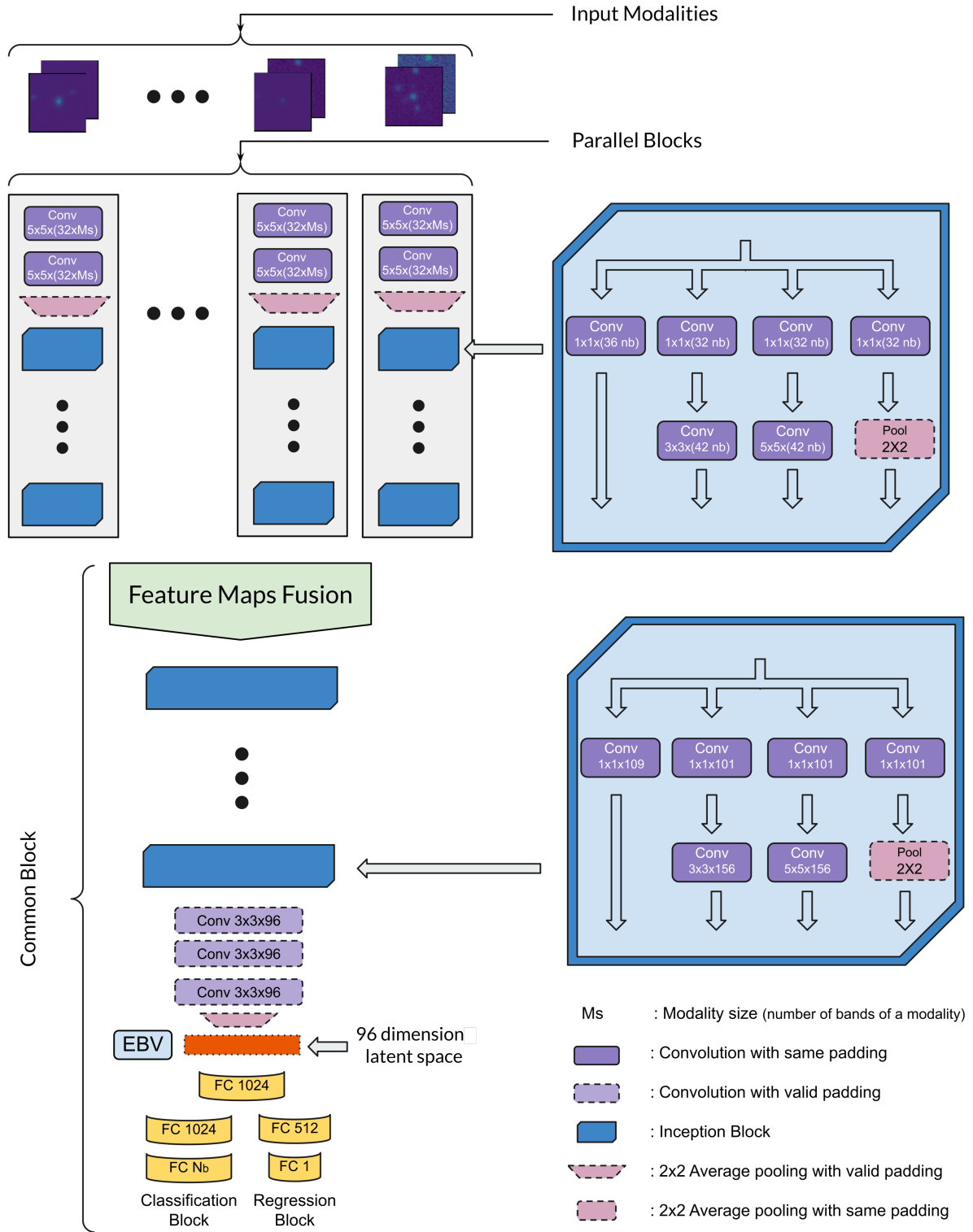


Fig. 1: Generic architecture of the multimodality network. The number of parallel blocks is contingent on the number of modalities. The depth of both the parallel and common blocks will be determined by the type of fusion being implemented (early, middle or late fusion), however, it is important to note that the total network depth is fixed at 8 (each modality will go through 8 inception blocks in total). The same goes for the average pooling layers, they are performed, consistently through the different architectures, before the 1st, 4th, and 6th inception blocks and the last one after the valid padding convolution layers. The baseline model without the multi modality approach represents a special case, where all the image bands are grouped into a single modality. The fixed depth allows for a standardized comparison between the different experiments.

3. Network and training procedure

3.1. Network input

For each galaxy, a $N \times 64 \times 64$ pixel data cube is created with subtracted background. N is the number of bands (5 for SDSS and CFHTLS, 6 or 9 for HSC-Deep). Images in the data cube are sorted in ascending order of wavelength (e.g. *ugriz*).

The network takes as input a batch of datacubes. Given the wide range of pixel values, the P19 dynamic range compression x_c is applied to each image, x , defined as $x_c = \text{sign}(x)(\sqrt{|x|+1}-1)$. Additionally, each band is center-reduced using all training objects. This ensures a more robust and efficient training.

Following P19, we also include as input the galactic reddening excess, $E(B-V)$, as the network has no information regarding the location of the sources. The $E(B-V)$ value is appended to the compressed non-spatial latent representation, helping to break the degeneracy between dust reddening and redshift (i.e., P19).

3.2. The baseline architecture

As a benchmark, we use a network architecture inspired by P19 and presented by Treyer et al. (2023), which delivers the currently best precision on the SDSS MGS dataset (Table. 2). The network consists of two convolutional layers followed by multiple sequential inception blocks (inspired from Szegedy et al. 2015). Each inception block is composed of convolutional layers, with different kernel sizes, which capture patterns at different resolutions. On all layers, a ReLU activation function (Nair & Hinton 2010) is used, with the exception of the first and second layers where a PReLU (He et al. 2015) and a hyperbolic tangent function are employed, respectively, to reduce the signal dynamic range. At the end of the sequential blocks, valid padding is applied, reducing the information to 96 one by one feature maps. Finally, sequential fully connected layers are employed to produce the classification and regression outputs.

3.3. Network output

The redshift estimation task has been treated using either a regression or a classification method. When a regression method is adopted, the network is trained by minimizing a loss function, e.g. the mean absolute error (MAE) or the root mean squared error (RMSE) between the predicted and true redshifts (Dey et al. 2021; Schuldt et al. 2021).

Alternatively, it can be treated using a classification method, as in P19 and in this work, and also in other kinds of applications (Rothe et al. 2018; Stöter et al. 2018; Rogez et al. 2017). We discretize the redshift space into narrow, mutually exclusive N_b redshift bins. The network is trained to classify each galaxy into the correct redshift bin through the optimization of the softmax cross-entropy (a strictly proper loss function). Gneiting & Raftery (2007) show that its correct minimization guarantees convergence to the true conditional probability.

The outputs of our non-linear, complex enough classification network (after the application of the softmax activation function) are positive and normalized scores distributed over the predefined redshift bins. We consider them estimators of the true conditional probability of the redshift belonging to a specific bin

(LeCun et al. 2015; Krizhevsky et al. 2017; Szegedy et al. 2015), which is, in turn, an approximation of the true redshift probability density function. Consequently, we will refer to the

network classification output as a redshift probability distribution (PDF).

In Appendix A, we show the performance obtained with models based on regression and/or classification methods using two different training sets. We find that the classification model outperforms the regression model. Additionally, we obtain a slight improvement by combining the classification and regression losses. In all subsequent experiments, we adopt this mixed scheme.

3.4. Network Training Protocol

We use an ADAM optimizer (Kingma & Ba 2014) and a batch size of 32 datacubes to train our network. Data augmentation is applied with random flips and rotations of the images (90° step).

The models are trained by simultaneously optimizing the cross-entropy loss function for the classification module and the MAE for the regression module. For a source s with spectroscopic redshift z_{spec} , the loss function is the sum of these two loss functions:

$$L(s) = \sum_{i=1}^{N_b} -y_i \log(p_i) + |z_{pred} - z_{spec}| \quad (1)$$

where N_b is the number of redshift classes, y_i the classification label of the redshift bin i (1 for the bin containing z_{spec} , 0 for the other bins), p_i the estimation for the class i produced by classification module and z_{pred} the regression estimate.

For a given training set, the database is split into 5 cross-validation samples. Each cross-validation sample (20%) is used as a test sample, while the remaining 4 (80%) are used for training. This guarantees that each galaxy appears once in the test sample. We use ensemble learning (Goodfellow et al. 2016) by running each training configuration several times with weights randomly initialized and the training set randomly shuffled: three times for the HSC and CFHTLS datasets and five times for the SDSS dataset (for comparison with other published works). The final PDF is the average of the outputs of the trained models.

All the results presented in the following sections are limited to $i \leq 24$.

4. Multimodality for redshift estimation

A key component of redshift estimation is the correlations between different bands covering different spectral domains. SED fitting techniques and machine learning algorithms exploit the flux ratios between bands. CNNs are able to capture correlations between different channels directly from the images and to extract spatially correlated patterns. In a classical CNN architecture, each kernel of the first convolution layer combines all the channels to produce one feature map (see Fig 3 in P19).

Multimodality is commonly used to train a network with multiple kinds of input data (i.e. images, audio, text) (Ngiam et al. 2011; Hou et al. 2018). Multiple input streams are incorporated into the network, processed in parallel and combined at a later stage (Hong et al. 2020). This allows for better feature extraction from each modality.

In the present work, we use multimodality to analyze subsets of bands separately before combining their outputs. In the following, we introduce our formalism for the multimodal configuration, the modifications to the network architecture and the key hyper-parameters involved in such networks.

4.1. Modalities

The images are sorted in ascending order of wavelength. The size of a modality refers to the number of bands it contains, while the order refers to the proximity of the bands. First-order modalities use adjacent bands, second-order modalities use bands separated by one band, third-order modalities use bands with a gap of two bands, etc. Table. C.2 details modalities of first, second and third order for the *ugrizyjhk* bands.

4.2. Network architecture

We adopt a flexible network architecture to incorporate the multimodalities. As illustrated in Fig. 1, we define two main parts:

- Parallel blocks : for each input modality, we define an independent module at the start of the network. It consists of successive inception blocks sized according to the size of the modality.
- Common block: it combines the outputs of the parallel blocks and proceeds with its own architecture detailed in Fig 1.

The depth of the parallel and common blocks depend on the type of fusion used as described in the next subsection. However we limit the total network depth to 8 inception blocks and the pooling layers are performed at fixed depths (before the 1st, 4th, and 6th inception blocks). The baseline architecture presented in section 3.2 can be obtained within the current framework by considering only one modality containing all the bands. In the following we use "baseline" and "baseline single modality" interchangeably.

4.3. Fusion

The stage of fusion, at which the parallel processed modalities are combined, is the last key factor to consider. It determines how much network processing is allocated to feature extraction from each modality and how much is assigned to combining those features for redshift estimation. We consider the following three stages (Hong et al. 2020):

- Early fusion: the features from each modality are fused after two parallel inception blocks, prior to passing through six common inception blocks.
- Middle fusion: modalities are combined after four parallel inception blocks, followed by four common blocks.
- Late fusion: modalities are combined after six inception blocks, followed by two common blocks.

We test two methods to fuse the feature maps from the different modalities: simple concatenation and cross-fusion. A cross-fusion module consists in a set of parallel inception blocks, each processing modalities one by one (hence cross) for improved feature blending. The cross-fused feature maps pass through a common convolution layer prior to being concatenated (Hong et al. 2020).

5. Experiments

5.1. Metrics and point estimates

To evaluate the photometric redshift performance between the different experiments, three metrics are considered based on the normalized residuals $\Delta z = (z_{\text{phot}} - z_{\text{spec}})/(1 + z_{\text{spec}})$ (P19):

- the **MAD** (Median Absolute Deviation), $\sigma_{\text{MAD}} = 1.4826 \times \text{Median}(|\Delta z - \text{Median}(\Delta z)|)$
- the fraction of **outliers**, η (%), with $|\Delta z| \geq 0.05$ for the SDSS or 0.15 for the other datasets.
- the **Bias**, $\langle \Delta z \rangle = \text{Mean}(\Delta z)$

We choose as point estimate, z_{phot} , the median of the output PDF. However this choice is not critical as we are interested in the relative performance of the various experiments.

5.2. Multimodality configurations

To evaluate the impact of the three variable ingredients of our multimodal approach, we use the HSC Deep Imaging Survey dataset (Section 2.3), as it covers the widest range of magnitude and redshift and has the largest number of photometric bands. We run experiments with different multimodal configurations in order to determine :

- the most efficient stage of fusion and the best fusion type between cross-fusion and simple concatenation,
- the optimal modality size,
- the optimal modality order,

for extracting redshift relevant information.

5.2.1. Stage and type of fusion

We conduct four experiments: early, middle, and late fusion with concatenation fusion, and an early cross fusion scenario, assuming size 2 and first and second order modalities.

The resulting MAD as a function of magnitude and redshift are shown in Fig. 2 and compared to the baseline, single modality model. Error bars are defined as the standard deviation between the metrics of the 5 validation folds. Early and middle fusions provide the most significant improvement with early fusion slightly outperforming middle fusion. The performance of the early concatenation fusion is similar to the early cross fusion scheme while being more computationally efficient. Thus we will proceed with concatenation fusion for the other experiments.

Additionally, we test very early fusion (where fusion occurs after the two initial convolutions and one inception block) and extremely early fusion (fusion after just two convolutions). Results reported in Fig B.4 show that early fusion obtains the best precision followed by very early fusion then extremely early fusion.

5.2.2. Size of modalities

We vary the size of the modalities from one to five assuming first order and early fusion. The MAD are presented in Fig. 3 as a function of magnitude and redshift. Adopting a size of 2 or more *significantly and* similarly improves the performance over the baseline. This confirms our initial hypothesis that processing subsets of bands in parallel prior to merging information helps the network to capture inter-band correlations. In contrast single band modalities perform similarly to the baseline at faint magnitude and worse at bright magnitude. The network may have more difficulties extracting inter-band correlation information, in this case not available until the modalities are merged within the network.

To further investigate these results, we analyze the impact of modalities of size 2 and 4 under early, middle and late fusion

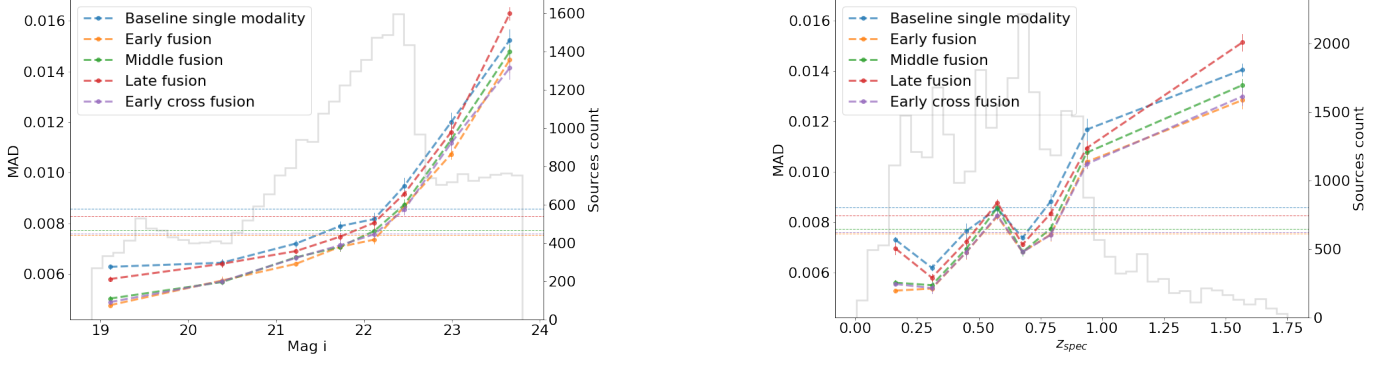


Fig. 2: MAD of the redshift estimation as a function of magnitude (i band, left panel) and spectroscopic redshift (right panel) for different types of fusion, compared to the baseline (single modality) model on the HSC 9-band dataset. The grey histograms represent the magnitude and redshift distributions, the horizontal lines show the mean MAD, and the error bars represent the standard deviation between the 5 validation folds. The data are split into 8 x-axis bins containing the same number of objects, each point representing the center of the bin.

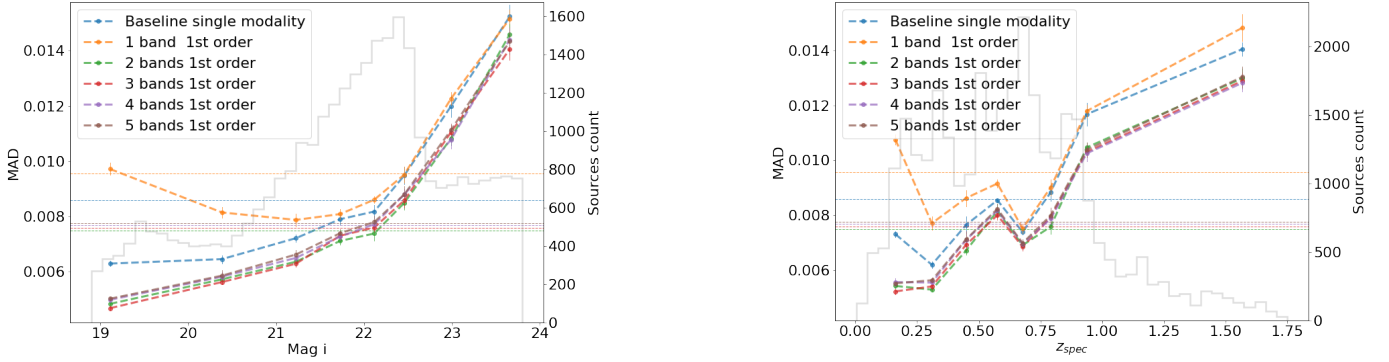


Fig. 3: Same as Fig 2 for early fusion, first order modality models with different number of bands per modality, compared to the baseline model.

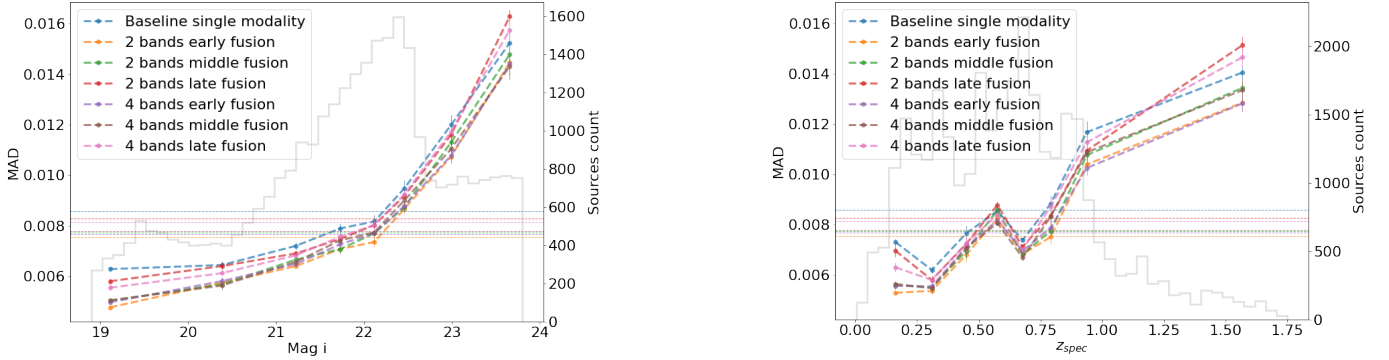


Fig. 4: Same as Fig 2 for modalities of size 2 and 4 using the three different stages of fusion, compared to the baseline model.

as shown in Fig. 4. We can observe the relatively minor impact of the modality size under the three different configurations. We conclude that the impact of modality size does not depend on the stage of fusion.

5.2.3. Order of modalities

Here we examine the impact of modalities based on the wavelength closeness of their bands. Assuming two-band modalities

and early fusion, we test four combinations of orders : first order; first and second; first, second and third order; and finally second and third order (the different orders are detailed in Table C.2).

As illustrated in Fig. 5, we find that experiments that included first order modalities performed optimally. The experiment using only second and third order was comparable to the baseline, showing that the network was not able to extract additional relevant inter-band correlation information that could outperform the baseline. These results are in line with expectations,

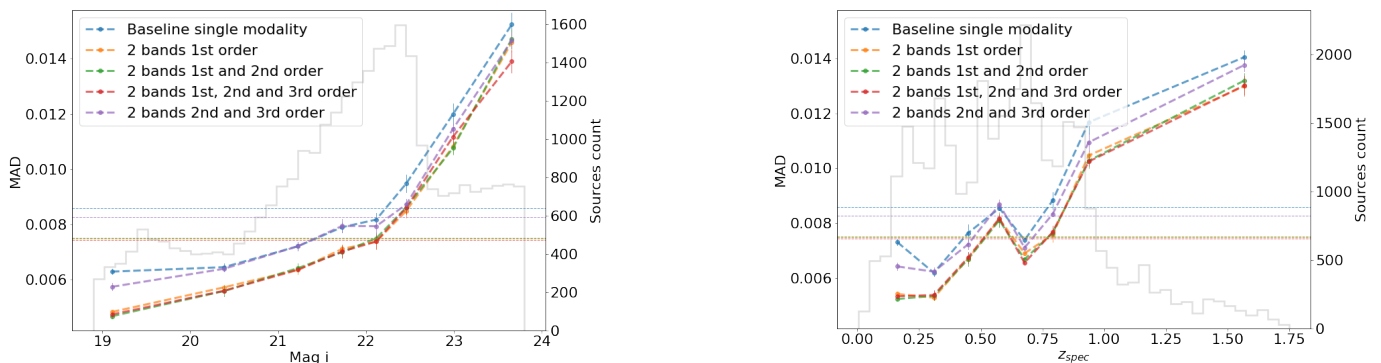


Fig. 5: Same as Fig 2 for different combinations of orders within 2-band modalities and using early fusion, compared to the baseline model.

Experiences	σ 10^{-3}	η %	$\langle \Delta z \rangle$ 10^{-3}
SDSS $r < 17.8$			
P19	9.08	0.31	0.04
Dey et al. (2021)	8.98	0.19	0.07
Hayat et al. (2021)	8.25	0.21	0.1
Treyer et al. (2023)	8.00	0.18	-0.31
Multimodal Network	7.85	0.16	0.31

Table 2: Performance comparison of different deep learning networks on the SDSS MGS ($r \leq 17.8$)

as adjacent bands express with the highest resolution the color information directly related to redshift estimation.

6. Results

Based on the above experiments, we evaluate the multimodal approach using two-band, first order modalities and performed cross-validations on different datasets.

The SDSS MGS dataset ($r \leq 17.8$) provides a benchmark to compare our work with other deep learning redshift estimates (P19; Dey et al. 2021; Hayat et al. 2021) and with the baseline model (Treyer et al. 2023). Results reported in Table. 2 show that the multimodal approach outperforms all previous works both in term of MAD and outlier fraction while not worsening the baseline bias.

We compare the multimodal network with the baseline on the CFHTLS (5 bands), and HSC (6 and 9 bands). Additionally, we test the network trained on the HSC 9 bands on the low resolution spectroscopic samples 3DHST and PRIMUS and on the high quality photometric redshift COSMOS2020. The metrics are reported in Table. 3. We also report the relative gain/loss defined as follows :

$$G(M) = \frac{|M_B| - |M_M|}{|M_B|} \quad (2)$$

where M_B and M_M are respectively the baseline and multimodality values of a given metric M . Finally, we estimate the statistical significance of the differences in metrics ($M_B - M_M$) using the paired bootstrap test detailed in Appendix D. The computed

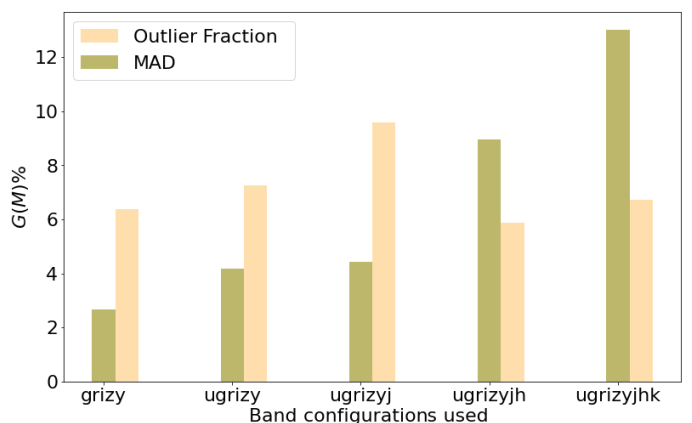


Fig. 6: Comparison of the multimodality gain $G(M)$ using 5, 6, 7, 8, and 9 bands for the MAD and outlier fraction on the HSC 9 band dataset

p values are reported in Table. 3 with statistically significant differences under a 5% risk threshold highlighted in green.

The results in Table 3 show that the multimodal approach offers statistically significant improvements of the MAD, ranging from 2% to 10%, across all datasets. In the case of 3DHST, the difference is significant under a 7% risk threshold. Similar improvements are also observed in the outlier fractions, ranging from 4% to 30%. However, the improvements in the HSC 9 and 6 bands and the 3DHST datasets were not statistically significant under a 5% risk threshold. Regarding the bias, the baseline approach performs better on the HSC 9 bands and CFHTLS, but with no significant difference. The two-band, first order setting achieves these results while being only 1.2 times slower than the baseline.

We investigate the relation between the impact multimodality and the number of bands. Figure 6 illustrates the multimodality gains compared to the baseline when training the models with different band combinations, specifically *grizy*, *ugrizy*, *ugrizyj*, *ugrizyjh*, and *ugrizyjhk*, using the HSC 9 band subset. We can see that the impact of multimodality on the MAD becomes more pronounced as more bands are incorporated into the training.

Its effect on the outlier fraction is less conclusive, as it does not exhibit a consistent pattern with the increasing number of bands.

In conclusion, our experiments show that the multimodality approach offers statistically significant improvement in the pre-

Experiences	σ 10^{-3}	η %	$\langle \Delta z \rangle$ 10^{-3}	Count 10^3
SDSS				
Baseline	07.99	0.18	0.34	516.5
Multimodal	07.85	0.16	0.31	516.5
$G(M)$	1.74%	10.88%	6.28%	-
$pvalue$	0.0	0.0	0.0	-
CFHTLS				
Baseline	16.01	0.85	0.22	108.5
Multimodal	15.35	0.79	0.29	108.5
$G(M)$	4.13%	7.22%	-24.05%	-
$pvalue$	0.0	0.0002	0.15	-
HSC-6b				
Baseline	09.14	1.25	1.97	46.8
Multimodal	08.87	1.20	1.63	46.8
$G(M)$	2.96%	3.94%	17.33%	-
$pvalue$	0.0	0.0575	0.04	-
HSC-9b				
Baseline	08.41	1.24	1.58	33.1
Multimodal	07.60	1.19	1.64	33.1
$G(M)$	10.1%	3.67%	-3.1%	-
$pvalue$	0.0	0.11	0.40	-
HSC-9b with 3DHST redshifts				
Baseline	14.44	2.46	13.28	2.2
Multimodal	13.88	2.37	10.6	2.2
$G(M)$	3.93%	3.71%	20.19%	-
$pvalue$	0.069	0.27	0.10	-
HSC-9b with PRIMUS redshifts				
Baseline	12.34	2.66	11.84	15
Multimodal	11.38	1.85	09.23	15
$G(M)$	7.74%	30.4%	22.01%	-
$pvalue$	0.0	0.0	0.0	-
HSC-9b with COSMOS2020 photometric redshifts				
Baseline	12.01	1.01	8.74	43.7
Multimodal	11.46	0.83	6.82	43.7
$G(M)$	4.57%	17.08%	21.97%	-
$pvalue$	0.0	0.0	0.0001	-

Table 3: Impact of multimodality on different datasets. The MAD, the outlier fraction and the bias are reported for the baseline and the multimodal models, alongside with the relative difference and the $pvalue$ as a measure of significance of the observed difference. The sizes of the datasets **down to** $i = 24$ are reported on the last column. For the 9 band experiments, some objects had the j band missing, so we used redshift estimations of models trained in those conditions.

cision of the redshift estimation. This is observed in both the MAD and the outlier fraction across all datasets. The impact is less conclusive for the mean bias.

7. Discussions

7.1. Dependence on network architecture

We evaluate the integration of multi-modality in three additional network architectures: a 5-layer CNN, a 10-layer CNN, and a 21-layer CNN. The impact of multimodality on the MAD of redshift estimates for these architectures, as well as the inception baseline, is depicted in Fig. 7. The results show a consistent improvement when multimodality is incorporated. Its impact was more substantial in the deeper networks compared to the shallower 5

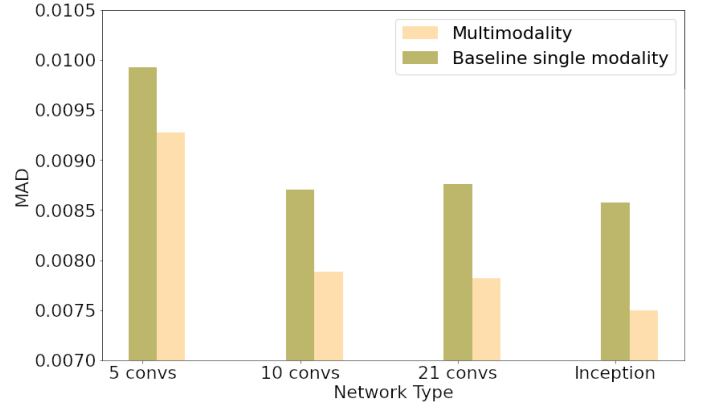


Fig. 7: Comparison of the multimodality impact on the MAD of the redshift estimation in the HSC 9-band dataset for 4 different network architectures.

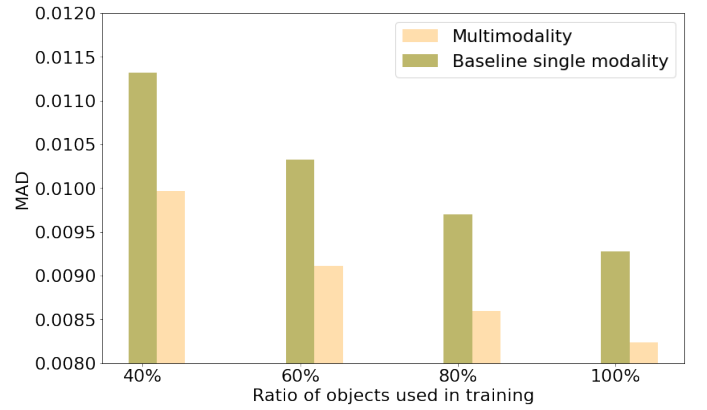


Fig. 8: Comparison of the multimodality impact on the MAD of the redshift estimation in the HSC 9-band dataset for four different sizes of the training set.

convolution layer network. We conclude that the effectiveness of multimodality is enhanced when the network architecture is sufficiently deep. Finally, we note that these results are unrelated to the number of network parameters as shown in Appendix C.

7.2. Dependence on training set size

We examined the effect of multi-modality for various sizes of training set using the HSC 9 band dataset. Fig. 8 presents the results when training on 40%, 60%, 80% and 100% of the training set. The results show that the multimodality improvement relative to the baseline remains consistent regardless of the training set size. We conclude that the effectiveness of multimodality is independent of the number of training objects.

7.3. Multimodality impact on training

The positive impact of multimodality can have different explanations. The most intuitive interpretation is that each parallel block that processes a subset of the input bands specializes in extracting information from the correlations between those bands, ultimately allowing the network to capture more relevant information than the baseline model.

Alternatively, noise may be present in the correlations between all the bands, causing an overfit. This noise would not

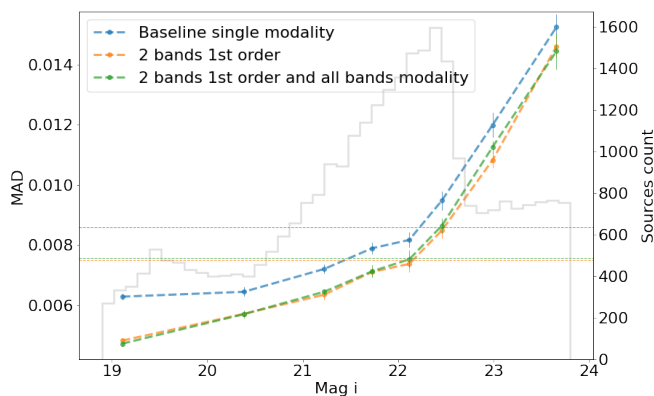


Fig. 9: MAD of the redshift estimation for two-band, first-order modalities with and without an additional modality containing all the bands, compared to the baseline model.

have a consistent relation with the redshift but the network could map it to the specific redshifts of the training sources, allowing it to optimize the training loss at the expense of extracting more general features. This would result in an under optimal performance on the validation set. Unlike the baseline, the multimodal network would avoid over-fitting this noise as the correlations between all the bands are not directly available, and so this optimization path would be more difficult to attain.

To investigate which of these two mechanisms better explains the observed gain, we design the following experiment using the HSC 9 band dataset: we add a new modality containing all 9 images to the existing modalities of the multimodal network. If the noise present in the correlation between the bands, which is preserved in the added modality, offers the easiest optimization path and facilitates over-fitting, we would expect the performance to degrade back to the baseline model. If, on the other hand, the benefit of multimodality arises from improved extraction of information, the additional modality should have little impact on the performance.

The results presented in Fig. 9 point to the latter option. We conclude that the multimodality approach gains from extracting more information rather than from reducing over-fitting.

7.4. Modality dropout

In order to study the impact of specific inter-band correlations on redshift estimation, we use a specific type of dropout technique, whereby the output of a given modality is entirely dropped, allowing us to weigh its relative importance on network performance. We aim to study the impact of the correlations between each two bands and not necessarily the bands themselves.

To do so, we train a network with two-band, first-order modalities and nine single-band modalities, to guarantee that no information is lost in the test phase when a 2-band modality is dropped. During the training phase, we randomly drop out from 0 to 5 modalities for each batch, while during the test, we consistently drop one specific modality.

Figure 10 shows how the test MAD is affected as a function of redshift. The models are ranked according to their impact on the mean MAD value. We also show for comparison the baseline model, our reference multimodal model and the multimodal model trained with modality dropouts, but tested with no modality dropped. The results can be summarized as follows:

- The network trained with dropouts but tested without performs similarly (marginally lower) to the reference multimodal model. It reflects that the classical model keeps a good level of generalization.
- When dropping only one single-band modality, the results are also very close to the reference multimodal model whatever the band dropped. This shows that the network focuses more on the two-band modalities, as we might expect.
- When dropping a 2-band modality, the impact is very dependant on which one is dropped. Modalities with optical bands, g_r and r_i , are overall the most important, with noticeable trends with redshift. The blue modality, u_g , is critical at low redshift $z \leq 0.5$, while j_h , i_z and z_y are more important at high redshift ($z \geq 1$).

To conclude, the modality dropout test allows us to confirm that our multimodal model retains a good level of generalization and to highlight the importance of specific pairs of bands at different redshifts, as do SED fitting methods but with much better accuracy.

8. Conclusion

We introduce multimodality as a novel approach for redshift estimation in the framework of supervised deep learning. The input consists of galaxy images in several broad band filters, labelled with a spectroscopic redshift. Subsets of bands (modalities) are first processed separately in parallel, their respective feature maps are then combined at an appropriate stage in the network and fed to a common block. We find that this technique enhances the extraction of color information independently of the network number of parameters and it *significantly* improves the redshift precision on various datasets covering a range of characteristics (depth, sky coverage, resolution). In particular, our approach achieves new state-of-the-art results on the widely used SDSS MGS dataset.

We explored modalities of different sizes and different wavelength proximity with different stages of fusion. We conclude that the early fusion of modalities composed of two adjacent bands offer the best results with minimal complexity.

Like other CNNs, our multimodal network fully exploits the information present at the pixel level but the prior parallel processing of bi-color modalities captures additional color information that improve its outcome. We find that the improvement in photometric redshift precision is statistically significant, does not depend on a specific CNN architecture, and that it increases with the number of photometric filters available. This scheme, combined with a modality dropout test, allows us to highlight the impact of individual colors on the redshift estimation as a function of redshift.

Future work will focus on leveraging the advancements made in this study to produce redshifts for the entire HSC dataset. This will present a number of challenges, such as domain mismatch between different multi-band image acquisition conditions and the scarcity of spectroscopically confirmed redshifts. Despite these challenges, the use of multimodality and other developed deep learning techniques have the potential to provide reliable estimates of photometric redshift, which will deliver valuable insights into the large-scale structure of the universe and the evolution of galaxies.

Acknowledgements. This work was carried out thanks to the support of the DEEPDIP ANR project (ANR-19-CE31-0023, <http://deepdip.net>), the Programme National Cosmologie et Galaxies (PNCG) of CNRS/INSU with INP

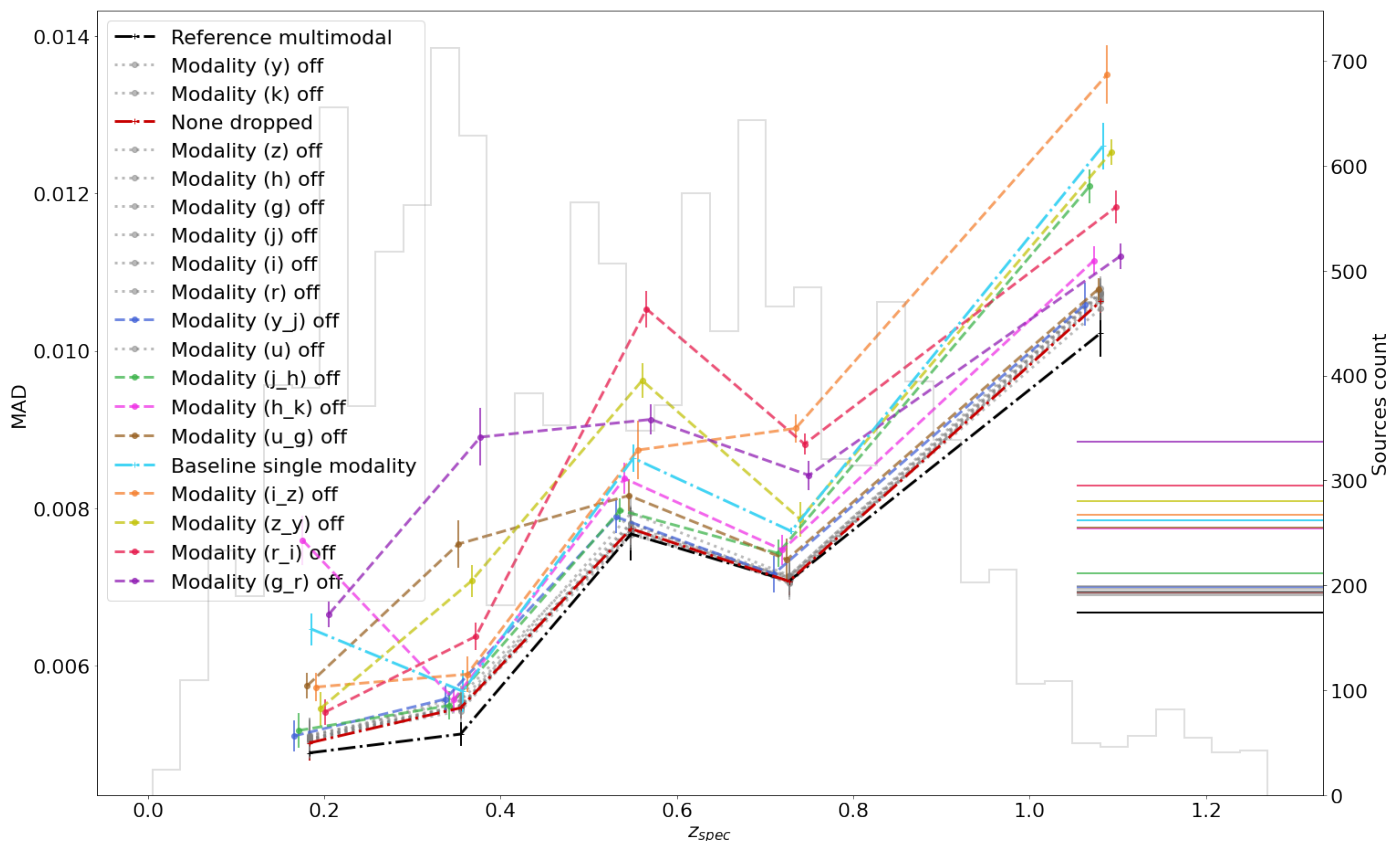


Fig. 10: Evolution of the MAD as a function of redshift for the multimodal model with one modality dropped at a time. All the single-band modalities dropped are shown with grey lines as they show similar performances. We also include, for comparison, the baseline model (single modality, cyan dot-dashed line), the reference multimodal model (black dot-dashed line) and the multimodal model trained with dropout but with no modality dropped in the test (dark red dot-dashed line). Finally, we have the different 2-band modalities dropped one at a time. Labels on the left panel are ranked according to their mean MAD. The grey histogram shows the redshift distribution of the HSC 9-band test sample. The test objects are evenly distributed between the line points which are slightly shifted on the x axis for better visual distinctiveness. The horizontal lines on the right represent the mean MAD for each experiment.

and IN2P3, co-funded by CEA and CNES.

This publication makes use of Sloan Digital Sky Survey (SDSS) data. Funding for SDSS-III has been provided by the Alfred P. Sloan Foundation, the Participating Institutions, the National Science Foundation, and the U.S. Department of Energy Office of Science. The SDSS-III web site is <http://www.sdss3.org/>. SDSS-III is managed by the Astrophysical Research Consortium for the Participating Institutions of the SDSS-III Collaboration including the University of Arizona, the Brazilian Participation Group, Brookhaven National Laboratory, Carnegie Mellon University, University of Florida, the French Participation Group, the German Participation Group, Harvard University, the Instituto de Astrofísica de Canarias, the Michigan State/Notre Dame/JINA Participation Group, Johns Hopkins University, Lawrence Berkeley National Laboratory, Max Planck Institute for Astrophysics, Max Planck Institute for Extraterrestrial Physics, New Mexico State University, New York University, Ohio State University, Pennsylvania State University, University of Portsmouth, Princeton University, the Spanish Participation Group, University of Tokyo, University of Utah, Vanderbilt University, University of Virginia, University of Washington, and Yale University. This publication makes use of the Canada France Hawaii Telescope Legacy Survey (CFHTLS) and CFHT Large Area U-band Deep Survey (CLAUDS), based on observations obtained with MegaPrime/MegaCam, a joint project of CFHT and CEA/IRFU, at the Canada-France-Hawaii Telescope (CFHT) which is operated by the National Research Council (NRC) of Canada, the Institut National des Science de l'Univers of the Centre National de la Recherche Scientifique (CNRS) of France, and the University of Hawaii. This work is based in part on data products produced at Terapix available at the Canadian Astronomy Data Centre as part of the Canada-France-Hawaii Telescope Legacy Survey, a collaborative project of NRC and CNRS.

CLAUDS use data from the Hyper Suprime-Cam (HSC) camera. The HSC instrumentation and software were developed by the National Astronomical Observatory of Japan (NAOJ), the Kavli Institute for the Physics and Mathematics of the Universe (Kavli IPMU), the University of Tokyo, the High Energy Acceleration

Research Organization (KEK), the Academia Sinica Institute for Astronomy and Astrophysics in Taiwan (ASIAA), and Princeton University. Funding was contributed by the FIRST program from Japanese Cabinet Office, the Ministry of Education, Culture, Sports, Science and Technology (MEXT), the Japan Society for the Promotion of Science (JSPS), Japan Science and Technology Agency (JST), the Toray Science Foundation, NAOJ, Kavli IPMU, KEK, ASIAA, and Princeton University. CLAUDS is a collaboration between astronomers from Canada, France, and China described in Sawicki et al. (2019) and uses data products from CALET and the Canadian Astronomy Data Centre (CADC) and was processed using resources from Compute Canada and Canadian Advanced Network For Astrophysical Research (CANFAR) and the CANDIDE cluster at IAP maintained by Stephane Rouberol.

References

- Ahumada, R., Prieto, C. A., Almeida, A., et al. 2020, *ApJS*, 249, 3
Aihara, H., AlSayyad, Y., Ando, M., et al. 2019, *PASJ*, 106
Alam, S., Albareti, F. D., Allende Prieto, C., et al. 2015, *ApJS*, 219, 12
Arnouts, S., Cristiani, S., Moscardini, L., et al. 1999, *MNRAS*, 310, 540
Baldry, I. K., Liske, J., Brown, M. J. I., et al. 2018, *MNRAS*, 474, 3875
Beck, R., Dobos, L., Budavári, T., Szalay, A. S., & Csabai, I. 2016, *MNRAS*, 460, 1371
Benítez, N. 2000, *ApJ*, 536, 571
Berg-Kirkpatrick, T., Burkett, D., & Klein, D. 2012, in *Proceedings of the 2012 Joint Conference on Empirical Methods in Natural Language Processing and Computational Natural Language Learning* (Jeju Island, Korea: Association for Computational Linguistics), 995–1005
Bertin, E. 2006, *Astronomical Data Analysis Software and Systems XV ASP Conference Series*, 351, 112

- Bertin, E. & Arnouts, S. 1996, *A&AS*, 117, 393
- Bertin, E., Mellier, Y., Radovich, M., et al. 2002, in *Astronomical Society of the Pacific Conference Series*, Vol. 281, *Astronomical Data Analysis Software and Systems XI*, ed. D. A. Bohlender, D. Durand, & T. H. Handley, 228
- Boulade, O., Charlot, X., Abbon, P., et al. 2000, in *Society of Photo-Optical Instrumentation Engineers (SPIE) Conference Series*, Vol. 4008, *Society of Photo-Optical Instrumentation Engineers (SPIE) Conference Series*, ed. M. Iye & A. F. Moorwood, 657–668
- Bradshaw, E. J., Almaini, O., Hartley, W. G., et al. 2013, *MNRAS*, 433, 194
- Brammer, G. B., van Dokkum, P. G., & Coppi, P. 2008, *ApJ*, 686, 1503
- Carliles, S., Budavári, T., Heinis, S., Priebe, C., & Szalay, A. S. 2010, *The Astrophysical Journal*, 712, 511
- Chen, Y., Li, C., Ghamisi, P., Jia, X., & Gu, Y. 2017, *IEEE Geoscience and Remote Sensing Letters*, 14, 1253
- Coil, A. L., Blanton, M. R., Burles, S. M., et al. 2011, *ApJ*, 741, 8
- Collister, A. A. & Lahav, O. 2004, *PASP*, 116, 345
- Cool, R. J., Moustakas, J., Blanton, M. R., et al. 2013, *ApJ*, 767, 118
- Csabai, I., Dobos, L., Trencsényi, M., et al. 2007, *Astronomische Nachrichten*, 328, 852
- Dalton, G. B., Caldwell, M., Ward, A. K., et al. 2006, in *Society of Photo-Optical Instrumentation Engineers (SPIE) Conference Series*, Vol. 6269, *Society of Photo-Optical Instrumentation Engineers (SPIE) Conference Series*, ed. I. S. McLean & M. Iye, 62690X
- de Jong, J. T. A., Kuijken, K., Applegate, D., et al. 2013, *The Messenger*, 154, 44
- Desprez, G., Picouet, V., Moutard, T., et al. 2023, *A&A*, 670, A82
- Dey, B., Andrews, B. H., Newman, J. A., et al. 2021, *arXiv e-prints*, arXiv:2112.03939
- Drinkwater, M. J., Byrne, Z. J., Blake, C., et al. 2018, *MNRAS*, 474, 4151
- Efron, B. & Tibshirani, R. J. 1994, *An introduction to the bootstrap* (CRC press)
- Emerson, J. P., Sutherland, W. J., McPherson, A. M., et al. 2004, *The Messenger*, 117, 27
- Garilli, B., McLure, R., Pentericci, L., et al. 2021, *A&A*, 647, A150
- Gneiting, T. & Raftery, A. E. 2007, *Journal of the American statistical Association*, 102, 359
- Goodfellow, I., Bengio, Y., & Courville, A. 2016, *Deep learning* (MIT press)
- Hayat, M. A., Stein, G., Harrington, P., Lukić, Z., & Mustafa, M. 2021, *ApJ*, 911, L33
- He, K., Zhang, X., Ren, S., & Sun, J. 2015, in *Proceedings of the IEEE international conference on computer vision*, 1026–1034
- Hong, D., Gao, L., Yokoya, N., et al. 2020, *IEEE Transactions on Geoscience and Remote Sensing*, 59, 4340
- Hou, J.-C., Wang, S.-S., Lai, Y.-H., et al. 2018, *IEEE Transactions on Emerging Topics in Computational Intelligence*, 2, 117
- Hudelot, P., Cuillandre, J. C., Withington, K., et al. 2012, *VizieR Online Data Catalog*, II/317
- Ilbert, O., Arnouts, S., McCracken, H. J., et al. 2006, *A&A*, 457, 841
- Ivezić, Ž., Kahn, S. M., Tyson, J. A., et al. 2019, *ApJ*, 873, 111
- Jarvis, M. J., Bonfield, D. G., Bruce, V. A., et al. 2013, *MNRAS*, 428, 1281
- Kingma, D. P. & Ba, J. 2014, *arXiv preprint arXiv:1412.6980*
- Koehn, P. 2004, in *Proceedings of the 2004 Conference on Empirical Methods in Natural Language Processing (Barcelona, Spain: Association for Computational Linguistics)*, 388–395
- Krizhevsky, A., Sutskever, I., & Hinton, G. E. 2017, *Communications of the ACM*, 60, 84
- Laureijs, R., Amiaux, J., Arduini, S., et al. 2011, *arXiv e-prints*, arXiv:1110.3193
- Le Fèvre, O., Cassata, P., Cucciati, O., et al. 2013, *A&A*, 559, A14
- Le Fèvre, O., Tasca, L. A. M., Cassata, P., et al. 2015, *A&A*, 576, A79
- LeCun, Y., Bengio, Y., & Hinton, G. 2015, *nature*, 521, 436
- Lee, K.-G., Krolewski, A., White, M., et al. 2018, *ApJS*, 237, 31
- Lilly, S. J., Le Fèvre, O., Renzini, A., et al. 2007, *The Astrophysical Journal Supplement Series*, 172, 70
- Ma, L., Lu, Z., Shang, L., & Li, H. 2015, in *Proceedings of the IEEE international conference on computer vision*, 2623–2631
- Masters, D. C., Stern, D. K., Cohen, J. G., et al. 2019, *ApJ*, 877, 81
- McCracken, H. J., Milvang-Jensen, B., Dunlop, J., et al. 2012, *A&A*, 544, A156
- McLure, R. J., Pearce, H. J., Dunlop, J. S., et al. 2013, *MNRAS*, 428, 1088
- Miyazaki, S., Komiyama, Y., Kawanomoto, S., et al. 2018, *PASJ*, 70, S1
- Momcheva, I. G., Brammer, G. B., van Dokkum, P. G., et al. 2016, *ApJS*, 225, 27
- Nair, V. & Hinton, G. E. 2010, in *Proceedings of the 27th international conference on machine learning (ICML-10)*, 807–814
- Newman, J. A., Cooper, M. C., Davis, M., et al. 2013, *ApJS*, 208, 5
- Ngiam, J., Khosla, A., Kim, M., et al. 2011, in *Proceedings of the 28th international conference on machine learning (ICML-11)*, 689–696
- Pasquet, J., Bertin, E., Treyer, M., Arnouts, S., & Fouchez, D. 2019, *A&A*, 621, A26
- Qian, K., Zhu, S., Zhang, X., & Li, L. E. 2021, in *Proceedings of the IEEE/CVF Conference on Computer Vision and Pattern Recognition*, 444–453
- Regnault, N., Conley, A., Guy, J., et al. 2009, *A&A*, 506, 999
- Rogez, G., Weinzaepfel, P., & Schmid, C. 2017, in *Proceedings of the IEEE Conference on Computer Vision and Pattern Recognition*, 3433–3441
- Rothe, R., Timofte, R., & Van Gool, L. 2018, *International Journal of Computer Vision*, 126, 144
- Sawicki, M., Arnouts, S., Huang, J., et al. 2019, *MNRAS*, 489, 5202
- Schlegel, D. J., Finkbeiner, D. P., & Davis, M. 1998, *ApJ*, 500, 525
- Schuldt, S., Suyu, S. H., Cañameras, R., et al. 2021, *A&A*, 651, A55
- Scodreggio, M., Guzzo, L., Garilli, B., et al. 2018, *A&A*, 609, A84
- Skelton, R. E., Whitaker, K. E., Momcheva, I. G., et al. 2014, *ApJS*, 214, 24
- Stöter, F.-R., Chakrabarty, S., Edler, B., & Habets, E. A. 2018, in *2018 IEEE International Conference on Acoustics, Speech and Signal Processing (ICASSP)*, IEEE, 436–440
- Szalay, A. S., Connolly, A. J., & Szokoly, G. P. 1999, *AJ*, 117, 68
- Szegedy, C., Liu, W., Jia, Y., et al. 2015, in *Proceedings of the IEEE conference on computer vision and pattern recognition*, 1–9
- Treyer, M., Ait-Ouahmed, R., Pasquet, J., et al. 2023, *Monthly Notices of the Royal Astronomical Society*, submitted
- Weaver, J. R., Kauffmann, O. B., Ilbert, O., et al. 2022, *ApJS*, 258, 11

Appendix A: Classification or regression

To study the impact of both classification and regression training strategies, we test different models on both the HSC 9 band and the CFHTLS datasets using the single modality scheme.

We test training the model with the regression module using three different losses :

- Root mean square-error (RMSE) :

$$RMSE = \sqrt{\text{mean}((z_{pred} - z_{spec})^2)}$$
- mean absolute error (MAE) :

$$MAE = \text{mean}(|z_{pred} - z_{spec}|)$$
- normalized MAE (NMAE, with the residuals normalized by the value of the label) :

$$NMAE = \text{mean}\left(\frac{|z_{pred} - z_{spec}|}{z_{spec} + 1}\right)$$

We test also a model trained solely with classification, and one aided by a MAE regression, by combining with equal weight the two loss functions in the training.

The results of these experiments are presented in Table. A.1

For the two datasets, the performances with the regression appear to depend on the choice of the loss function, with the normalized MAE leading to the best performances. Overall the classification-based models outperform the regression ones (especially for the MAD) for both datasets independently of the depth and number of available bands. It is even slightly improved when the classification is co-optimized with a regression for the HSC dataset (we use the classification module estimation in this case).

As a conclusion, we adopt a classification model aided by a regression for all the experiments presented in this work.

Experiences	σ 10 ⁻³	η %	$< \Delta z >$ 10 ⁻³
HSC 9 bands			
Classification and Regression MAE	08.36	1.24	0.68
Classification	08.66	1.33	1.20
Regression RMSE	18.99	1.33	1.86
Regression MAE	13.04	1.26	1.57
Normalized Regression MAE	12.03	1.25	1.15
CFHTLS			
Classification and Regression MAE	16.28	0.99	1.43
Classification	16.28	0.98	1.46
Regression RMSE	20.79	0.96	1.18
Regression MAE	18.26	0.99	1.10
Normalized Regression MAE	17.95	0.99	-0.56

Table A.1: Global performances of classification and regression based models (see text) for the HSC 9 bands and CFHTLS dataset.

Appendix B: Multimodality impact on outlier fraction and bias

We previously detailed, for the different multimodality experiences, their impact on the MAD metric. Here we show the evo-

lution of the outlier fraction and bias as a function of the i band magnitude and the estimated redshift z_{pred} . We can see in the Figures B.1, B.2, B.3 that different multimodality configurations slightly improve outlier fraction and have little impact compared to the baseline model on the bias.

Appendix C: Configuration details

Table C.1 shows the number of parameters for various experiments. We can note that certain multimodal models outperformed the baseline while having a lower number of parameters like the 2-band first-order modalities with early fusion. Additionally, other models with a higher number of parameters, such as the 5-band first-order modalities with early fusion, also showed improved performance. These results reinforce our conclusion that the effectiveness of the multimodal approach relies not on the number of parameters but rather on its superior capacity of relevant information extraction.

Table C.2 details the composition of the modalities of first, second and third order and sizes of two, three and four bands per modality when using the *ugrizyjhk* bands.

Experience	Parameters (10 ⁶)
Baseline	19.03
2 bands first order	
Extremely early fusion	9.52
Very early fusion	11.16
Early fusion	12.51
Middle fusion	15.22
Late fusion	17.94
Early fusion first order	
1 band	8.80
2 bands	12.51
3 bands	17.23
4 bands	22.11
5 bands	26.29
Early fusion 2 bands	
1st and 2nd order	17.37
1st, 2nd and 3rd order	21.54
2nd and 3rd order	15.98

Table C.1: Number of trainable parameters for some models grouped by fusion stage, modality size and modalities' orders.

	2 bands	3 bands	4 bands
1st order	u_g, g_r, r_i, i_z, z_y, y_j, j_h, h_k	u_g_r, g_r_i, r_i_z, i_z_y, z_y_j, y_j_h, j_h_k	u_g_r_i, g_r_i_z, r_i_z_y, i_z_y_j, z_y_j_h, y_j_h_k
2nd order	u_r, g_i, r_z, i_y, z_j, y_h, j_k	u_r_z, g_i_y, r_z_j, i_y_h, z_j_k	u_r_z_j, g_i_y_h, r_z_j_k
3rd order	u_i, g_z, r_y, i_j, z_h, y_k	u_i_j, g_z_h, r_y_k	

Table C.2: A detailed breakdown of the specific bands that are included in each modality for all the first, second, and third order modalities of sizes 2, 3, and 4 in a 9 band dataset.

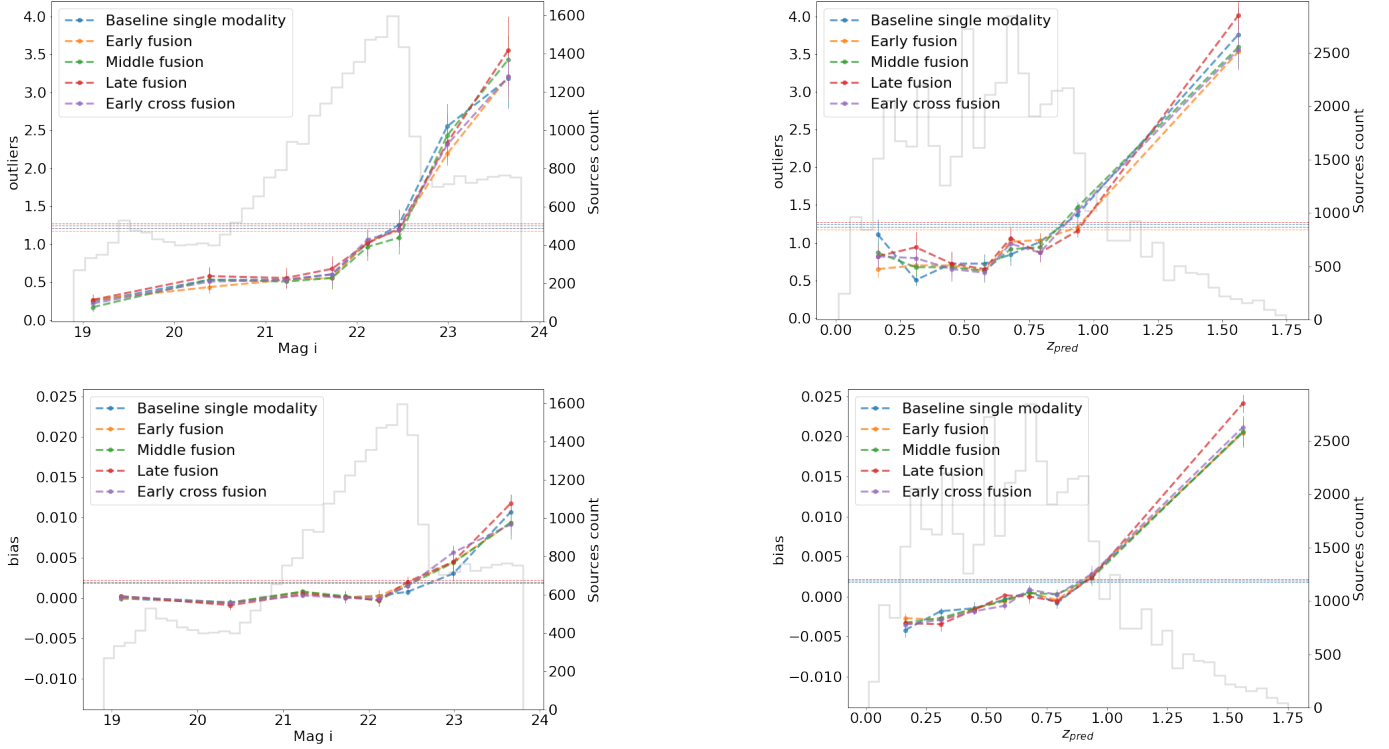


Fig. B.1: Comparison of the outlier fraction and bias versus band i magnitude and predicted redshift for different fusion types and the single modality baseline on the 9-band sources from the HSC dataset

Appendix D: Paired bootstrap test

To assess the statistical significance of the observed difference between the baseline and the multimodal approaches, we use the paired bootstrap significance test introduced by Efron & Tibshirani (1994) and frequently used in the field of natural language processing (Berg-Kirkpatrick et al. 2012; Koehn 2004). It is a non-parametric hypothesis test with no assumption about the distribution of the data. For a given dataset, D , we define:

$$\delta(D) = M_M(D) - M_B(D) \quad (\text{D.1})$$

where $M_M(D)$ and $M_B(D)$ are the metrics of the multimodal and the baseline model respectively for the dataset D . We first assume that M_M is, contrary to what we believe, equal or worse than M_B . This is known as the null hypothesis, H_0 . Next, for a given dataset D_{test} , we estimate the likelihood, $p_{value}(D_{test})$, of observing, under H_0 and on a new dataset D , a metric gain $\delta M(D)$ equal to or better than $\delta M(D_{test})$, so that :

$$p_{value}(D_{test}) = P(\delta(D) \geq \delta(D_{test}) | H_0) \quad (\text{D.2})$$

A low $p_{value}(D_{test})$ suggests that observing $\delta(D_{test})$ is unlikely if H_0 was true, so we can reject H_0 and conclude that the metric gain $\delta(D_{test})$ of M_M compared to M_B is significant and not just a random fluke.

The $p_{value}(D_{test})$ is hard to compute and must be approximated as we don't have new data sets to test on, so we use the paired bootstrap method to simulate this. We sample from the test set, with replacement, K same size samples as the test set, on which $\delta(D_{test})$ was computed. We refer to these samples as bootstrapped samples.

Naively we may think that we should compute the frequency of $\delta(D_{bootstrapped}) \geq \delta(D_{test})$ over the K samples as an approximation of $p_{value}(D_{test})$. However, these samples won't be suitable for our null hypothesis H_0 since they were sampled from the test set, causing their average $\delta(D_{bootstrapped})$ to be around $\delta(D_{test})$ contrary to what H_0 requires. Because H_0 assumes that the initially observed difference $\delta(D_{test})$ is due to a random fluke, the solution is to shift the $\delta(D_{bootstrapped})$ distribution by this value, so we obtain:

$$p_{value}(D_{test}) = \text{Freq}(\delta(D_{bootstrapped}) - \delta(D_{test}) \geq \delta(D_{test})) \quad (\text{D.3})$$

The results reported in Table. 3 are obtained with a significance test assuming $K = 10^4$.

Fig. D.1 illustrates two cases for the HSC 9 band dataset: the left panel shows the distributions for the MAD of the bootstrapped samples, where the performance gain is significant; the right panel shows the distributions for the outlier fractions where the gain is not significant under a 5% risk threshold. The green histogram is the original distribution that does not satisfy H_0 , the red histogram is the shifted one that satisfies H_0 . The blue line represents the difference initially observed on the test dataset $\delta(D_{test})$, and the $p_{value}(D_{test})$ corresponds to the fraction of the red histogram exceeding this value.

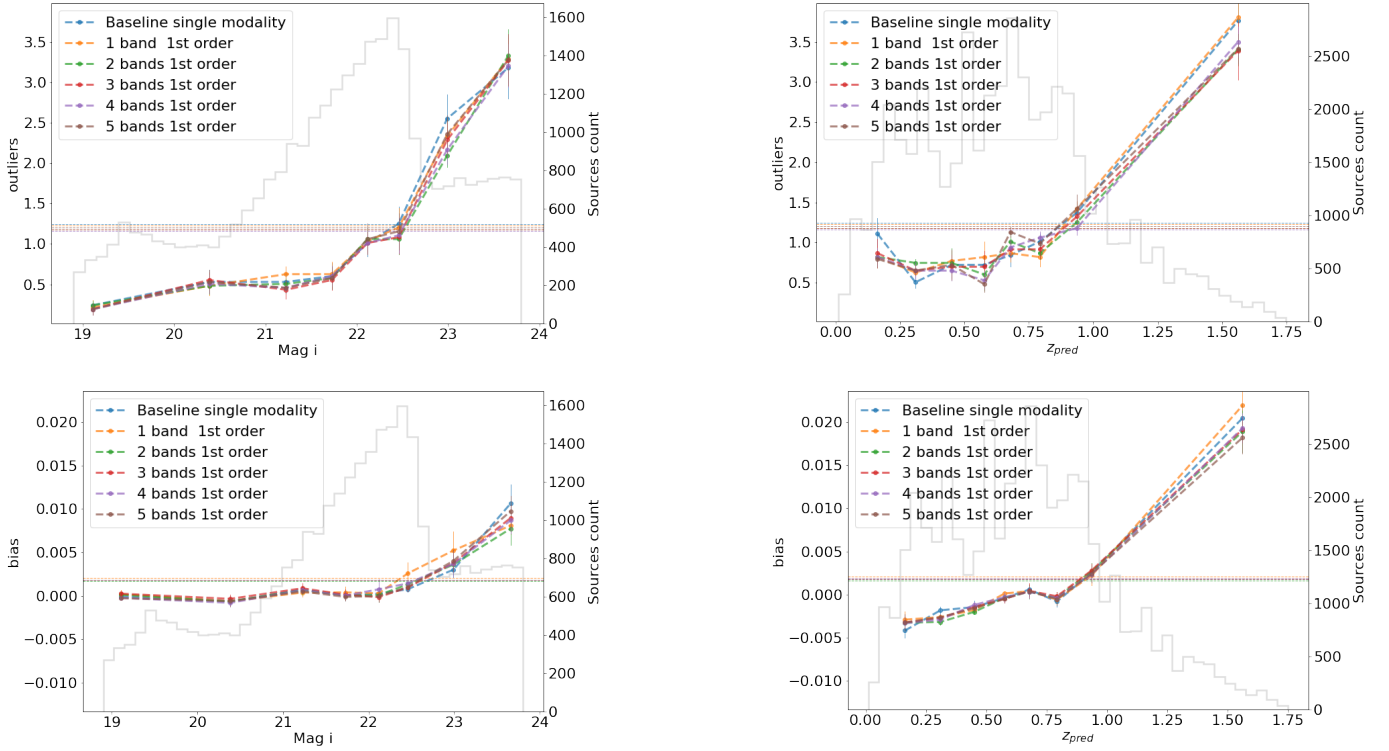


Fig. B.2: same as Fig B.1 for early fusion first order modalities models with different number of bands per modality and the single modality baseline.

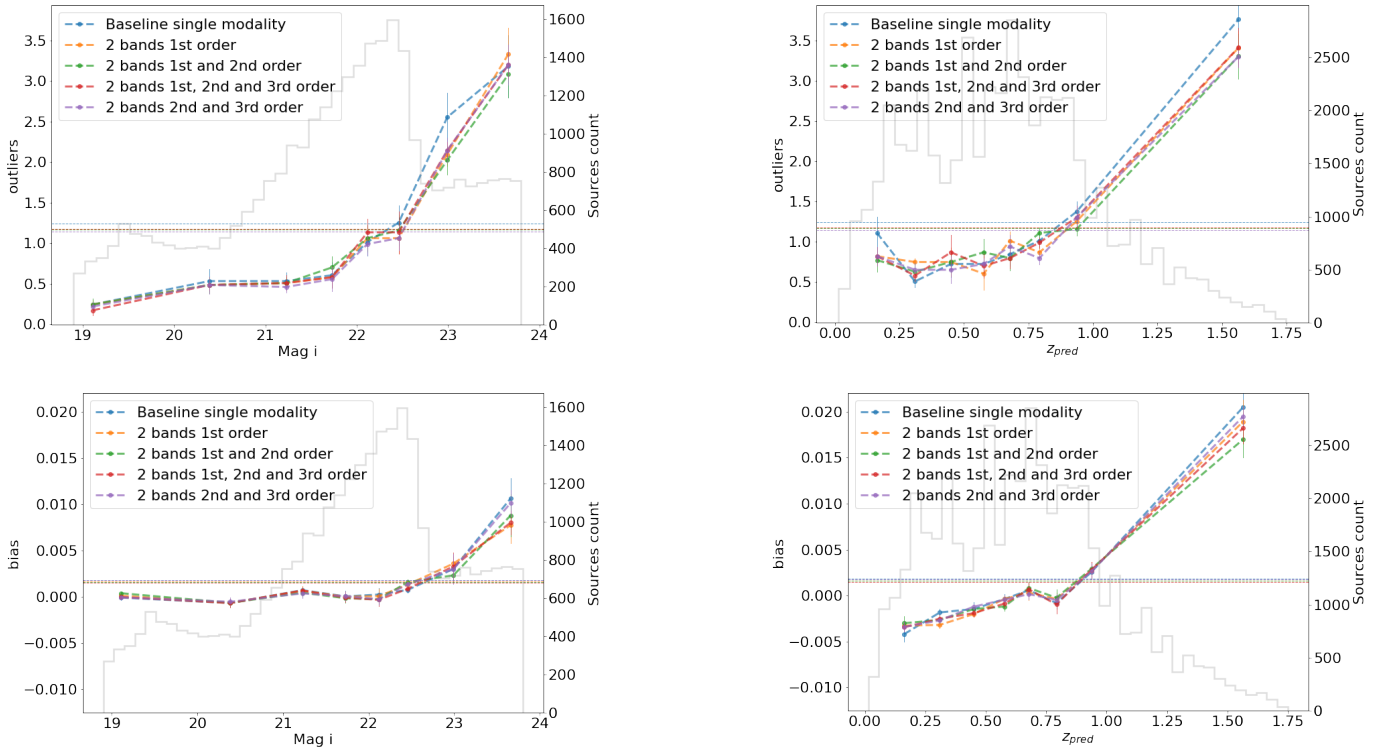


Fig. B.3: Same as Fig B.1 for different modality order combinations for 2 band modalities using early fusion and the single modality baseline.

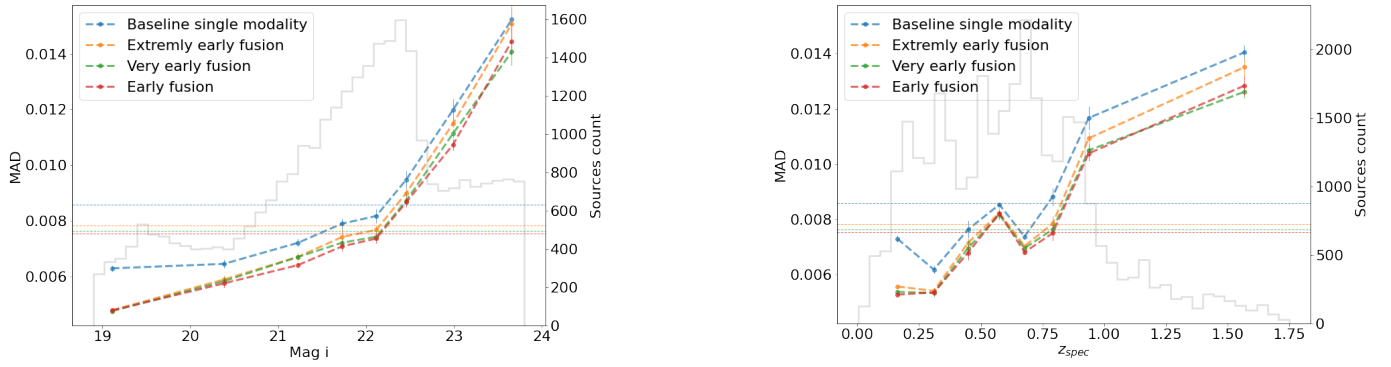


Fig. B.4: Same as Fig 2 for early, very early and extremely early fusion models and the baseline model.

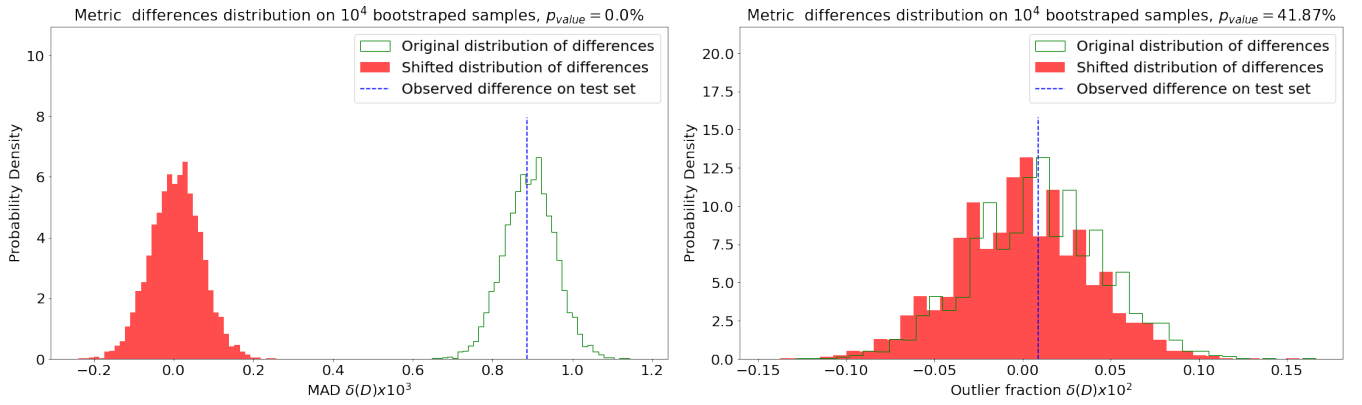


Fig. D.1: Distribution of the MAD and outlier fraction differences for a $K = 10^4$ paired bootstrap test to assess the significance of the difference between M_M and M_B on the HSC 9 band test dataset.